A concept for defining the mixed-mode behaviour of tough epoxy film adhesives by single specimen design

Jokinen, J[a,1], Orell, O[a], Wallin, M[b], Kanerva, M[a]

[a]*Tampere University, Materials Science and Environmental Engineering, PO Box 589, FI-33101 Tampere, Finland*
[b]*Patria Aviation, Lentokonetehtaantie 3, FI-35600 Halli, Finland*

Abstract

Fracture modes I and II interact in mixed-mode loading conditions, and the interaction is typically taken into account using a mixed-mode fracture criterion. In this work, a concept for defining the criterion is developed through an experimental-numerical simulation analysis. The mixed-mode behaviour for the criterion is tested and analysed with a single specimen design. The design of the specimen simplifies the measurement when complex test arrangements and preparations for various specimen geometries are excluded in practice. Here, the mixed-mode fracture behaviour of the specimen is analysed in detail using digital image correlation (DIC). The DIC data is used in collaboration with a finite element–based crack onset analysis, including the virtual crack closure technique, in order to consider the typical simplifications and their effects on the mixed-mode criterion. As a benchmark case, the fracture criterion is determined for an epoxy film adhesive FM 300-2 using the developed approach. The developed approach was shown to be feasible and effective for defining the mixed-mode fracture criterion. The determined Power law criterion's exponents were below unity, which points out that the common (presumed) exponent values in the current literature are actually unconservative.

[1] Corresponding author.

Email address: Jarno.Jokinen@tuni.fi (Jokinen, J)

Keywords: adhesive, mixed-mode testing, epoxy, virtual crack closure technique, digital image correlation

1. Introduction

Adhesively bonded joints are typically designed to carry shear loads. This type of pure single-mode loading can be computationally analysed by comparing the energy release rate (ERR) – provided by the selected numerical analysis – to the critical ERR provided by the experiments. A pure single-mode loading is scarce in real applications, where joints will also meet peeling loads, e.g., loads that typically exist at the edges of the joints. The actual loading in the adhesive layer is a combination of both peeling and shearing loads. The interaction of mode I and II can cause failure to occur when total ERR is less than critical value of either modes [1]. Shearing and peeling fracture modes have an interaction which is taken into account by using an adjusted mixed-mode fracture criterion. Several mixed-mode fracture criteria have been developed [2, 3, 4]. One of the most typical fracture criteria is the power law. The power law is typically formulated using only two fracture modes (I and II). The power law is commonly implemented in the commercial finite element (FE) codes, such as Abaqus [5]. The power law criterion can be extracted in the following form:

$$\left(\frac{G_I}{G_{IC}}\right)^{\alpha} + \left(\frac{G_{II}}{G_{IIC}}\right)^{\beta} = 1 \qquad (1)$$

where G_I and G_{II} are the ERRs evaluated in the analysis of the joint and G_{IC} and G_{IIC} are critical ERRs determined for the adhesive (layer). The parameters α and β are the fitting parameters.

The mixed-mode criterion is an equation which is fitted based on experimental results. The experimental methods for describing pure single fracture modes (I and II) have been developed and are essentially standard. A test using a double cantilever beam (DCB) specimen is the standard test method for mode I testing [6]. The methods for mode II testing include end-notched flexure (ENF), an end-loaded split (ELS),tapered end notched flexure (TENF) and end loaded shear joint (ELSJ) [7]. Standardised methods do not exist for fracture mode III.

The determination of the criterion (fitting) parameters requires experiments describing the mixed-mode behaviour. The mixed-mode testing for composite delamination is typically performed using mixed-mode bending (MMB) apparatus [8]. The MMB apparatus allows changing the mixed-mode ratio between modes I and II. Currently, no mixed-mode standard exists for adhesive testing. Various mixed-mode test specimens have been used for adhesives in the current literature and they include: an asymmetric tapered DCB specimen [9], a fixed-ratio mixed mode (FRMM) specimen [10], a mixed-mode flexure (MMF) specimen [10], an Arcan-type specimen [11, 12] and a single leg bending (SLB) specimen [13]. The different mixed-mode specimens in a loaded condition are visualised in Fig. 1 for clarity.

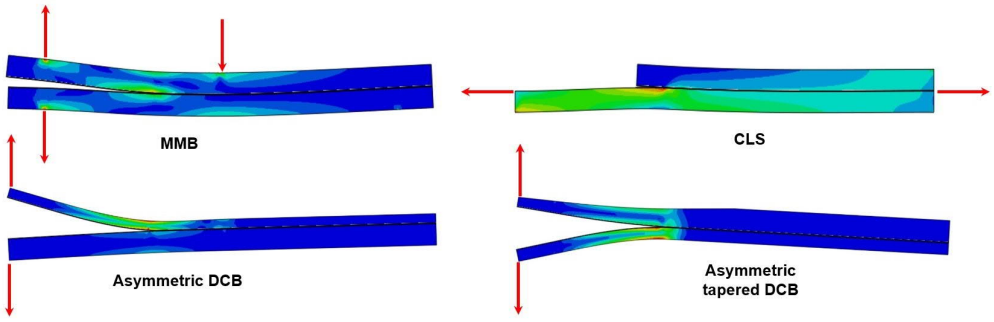

Figure 1: Different mixed-mode specimens in a typical loading condition. The colour range illustrates the estimative load intensity (von Mises).

In this work, a concept for defining the mixed-mode behaviour by using a single-specimen design, mainly based on SLB geometry, is developed. The test method is based on a simple three-point bending test setup, instead of using complex testing apparatus. The developed concept is applied for defining the mixed-mode fracture criterion for a structural, highly toughened epoxy film adhesive (FM 300-2 by Cytec). In addition to the mixed-mode testing, mode II (ENF) tests were performed for the selected adhesive. The mode I (DCB) results for the joints (FM 300-2) have been published in our previous work [14] and are the reference for the mode I results.

In addition, the mixed-mode deformation at the crack is studied in detail using the digital image correlation (DIC) method. The deformation is studied in terms of peel and shear strains. Strains are widely used for defining the sustainability limits of adhesive in the design of intact joints. The adhesive properties are typically defined under pure shear with a thick-adherend lap

shear (TALS) specimen. The target of applying the DIC was to verify the mixed-mode condition and provide an estimate for the maximum strains near the crack. The post-processing of test results via the ERR basis are performed with the virtual crack closure technique (VCCT), and a comparison of the adhesive behaviour amidst the crack tip is performed on a micro-meso length scale. The DIC results are compared with the numerical results for defining the representativeness of the DIC and the post-processing method.

2. Materials and methods

2.1. Materials and test specimens

ENF and SLB test specimens were prepared for the testing of this study. The materials of the specimens were identical for all of the specimen series. The specimen adherends were machined out from an aluminium alloy plate (Alumec 89, Uddeholm). The nominal thickness of the aluminium plate was 15 mm and 15.7 mm for ENF and SLB specimens respectively. The Young's modulus of 71 GPa and Poisson's ratio of 0.3 were used in all of the analyses for the aluminium. The epoxy film adhesive FM 300-2 (Cytec) was used in all of the specimens and the properties were estimated using the work carried out by Ishai et al. [15], who studied the adhesive FM 300 (Cytec). The values of 2.45 GPa and 0.38 were used for the Young's modulus and the Poisson's ratio respectively. Jokinen et al. [14] defined that the fracture toughness value of G_{Ic} = 1820 J/m^2 for the adhesive FM 300-2 should be used when determining the fracture criterion.

The dimensions of the test specimens are shown in Figs. 2–3. The average widths of the SLB and ENF specimens were 20.10 mm and 16.94 mm (measured) respectively. The average adhesive thickness of the ENF, SLBa and SLBb specimens were 0.71 mm, 0.40 mm and 0.67 mm respectively. Both specimens were fabricated using two adhesive plies, and the pre-existing crack was applied between the adhesive plies, as shown in Figs. 2–3. The adhesive thickness of the prepared SLBa specimens was determined to be lower than the other specimens. The manufacturing process was identical for all the specimens but the scatter in the processing devices and practical preparations resulted in 27 % deviation in the actual value of adhesive thickness (average SLBa thickness 0.4 mm and average SLB thickness 0.67 mm). The average pre-crack lengths of the ENF, SLBa and SLBb specimens were 107.88 mm, 24.63 mm and 29.48 mm respectively. The geometry for SLBa and SLBb specimens are the same, but the loading direction is opposite.

The pre-treatment of the adhesive bonding was performed using Sol-Gel handling [16], and finally, the adhesive was cured in an oven (120 °C) under a vacuum bag. The bonding was performed by joining larger plates, which were water-jet cut to the final specimen width after curing. Two identical test series of SLB specimens were formed, which are referred to as SLBa and SLBb later in this study.

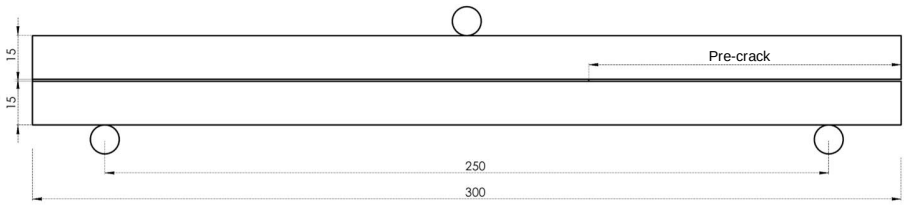

Figure 2: ENF specimen testing and the dimensions applied in this study.

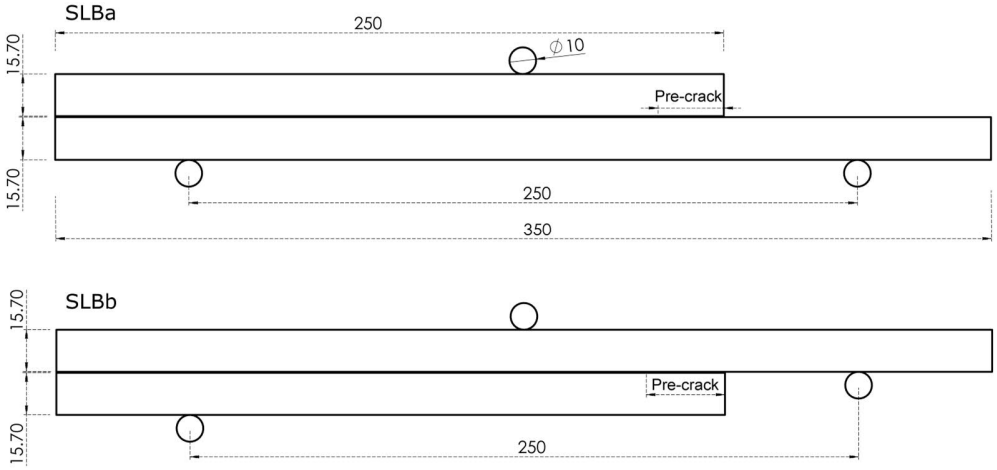

Figure 3: SLBa and SLBb specimen testing and the dimensions applied for the tests in this study.

2.2. Experimental testing

The ENF testing was performed using a universal testing machine (Dartec, 100 kN) with the three-point bending setup. The displacement in the specimen middle point was measured using an auxiliary displacement transducer (WA-T 20 mm, HBM). The SLB tests were performed with a

universal testing machine (5967, Instron, 30 kN). The tests of SLBa and SLBb were carried out with the three-point bending jig with the support and loading cylinders having a diameter of 10 mm. For the SLBb test, the support jig was modified for maintaining the horizontal orientation of the specimen. The difference between the tests are shown in Fig. 3. The crosshead displacement rate was 2 mm/min and the test programme for the SLBa and SLBb tests consisted of a constant loading and unloading steps corresponding to 4 mm and 3 mm midpoint deflection respectively. The load and the crosshead displacement data were collected with the integrated software (BlueHill 3, Instron). The strain at the bottom surface of the SLB specimen (below the loading cylinder) was measured using a foil strain gauge (5 mm gage length by Kyowa [Japan]) connected to Labview SignalExpress software (National Instruments). The SLBa test arrangement is presented in Fig. 4.

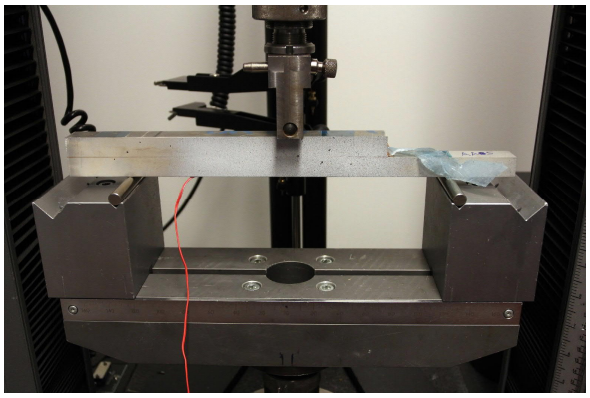

Figure 4: The SLBa testing set-up including the three point bend pins and a specimen with a strain gauge. The specimen is also provided with a speckle pattern for DIC.

2.3. DIC and the determination of adhesive deformations

In a typical DIC technique, the studied surface is divided into small facets (i.e. subsets) whose movements are then tracked from image to image. A subset needs to have enough unique features to be distinguished from other subsets, which is normally accomplished by applying some random speckle pattern on the surface. The precision and spatial resolution of the DIC analysis largely depend on the used subset and step sizes. The position of the centre point of each subset can be determined, and the density of the computed points is controlled by the step size. Finally, a full displacement

field can be determined, from which further strain fields can be calculated. [17]

In heterogeneous structures, such as the ones consisting of materials with very different mechanical properties, high spatial resolution is often needed in order to be able to measure the deformation gradients accurately. In many cases, by decreasing the subset size, the spatial resolution can be increased but, simultaneously, the precision of the quantity of interest (e.g. the displacement or strain) will decrease and vice versa. The maximum spatial gradient that the DIC system can resolve depends on, amongst other things, the image scale offered by the test set-up (or the final pixel-to-mm ratio), the speckle size of the used pattern, and the subset and step sizes when carrying out the analysis. [18, 19]

Here, the three-dimensional DIC technique was used to determine the full-field displacements and strains during the SLB tests. The system consisted of two 5 Mpix cameras (Imager E-Lite, LaVision), with the objectives having the focal length of 50 mm, and synchronized LED flashes, controlled with Davis 8.4 software (LaVision). The recording rate was 2 Hz. The scale factor with the used test configurations ranged between 22–25 pix/mm. The correlation analysis was performed using subset and step sizes of 25 pix and 7 pix respectively. The subset in the performed analysis corresponded approximately a 1 mm x 1 mm square in the test coordination, resulting in the applied DIC setup not directly offering a spatial resolution that was high enough for the detailed quantitative analysis of the deformations measured in the thin adhesive layer (t<0.7 mm) of the specimens.

However to overcome this, the shear and opening deformations of the bond line were determined with the following approach. It is assumed that the adherend behaviour is purely elastic during the given loading (Section 2.2), where the normals of the neutral axis of the specimen remain normals in the deformed state. First, the displacement vectors at the adherends of the loaded specimen are determined along the length of the sample (in the x-direction) at three different distances (here 1, 2 and 10 mm) from the midline of the adhesive layer. The constant n presents the ordinal of the exported DIC displacement vectors where n = 1 equals the location at the pre-crack. A line is fitted using these three points by the least squares method for each x-coordinate location (n). The fitted lines p_n and p'_n are presented in Fig. 5, where the points $\boldsymbol{A_n}$-$\boldsymbol{C_n}$ are the points in the undeformed upper adherend at

the n^{th} location, and the points $\boldsymbol{A'_n}$ - $\boldsymbol{C'_n}$ are then the same points in the deformed state.

When the location of the adhesive mid-line is known in the x-y plane (the origin at the pre-crack observed in the DIC images), the length of the vector $\boldsymbol{O_n}$ can be expressed as

$$\|\boldsymbol{O_n}\| = \|\boldsymbol{P_n}\| = L_0 \tag{2}$$

During the loading of the specimen, the compressive and shear strains in the metal adherend, near the epoxy adhesive, remain small and it is assumed that L_0 remains constant throughout the test. In the deformed state, the location of the point $\boldsymbol{Q'_n}$ is then given as:

$$\boldsymbol{Q'_n} = \boldsymbol{C'_n} + \boldsymbol{P_n} \tag{3}$$

where vector $\boldsymbol{P_n}$ is parallel to line p'_n.

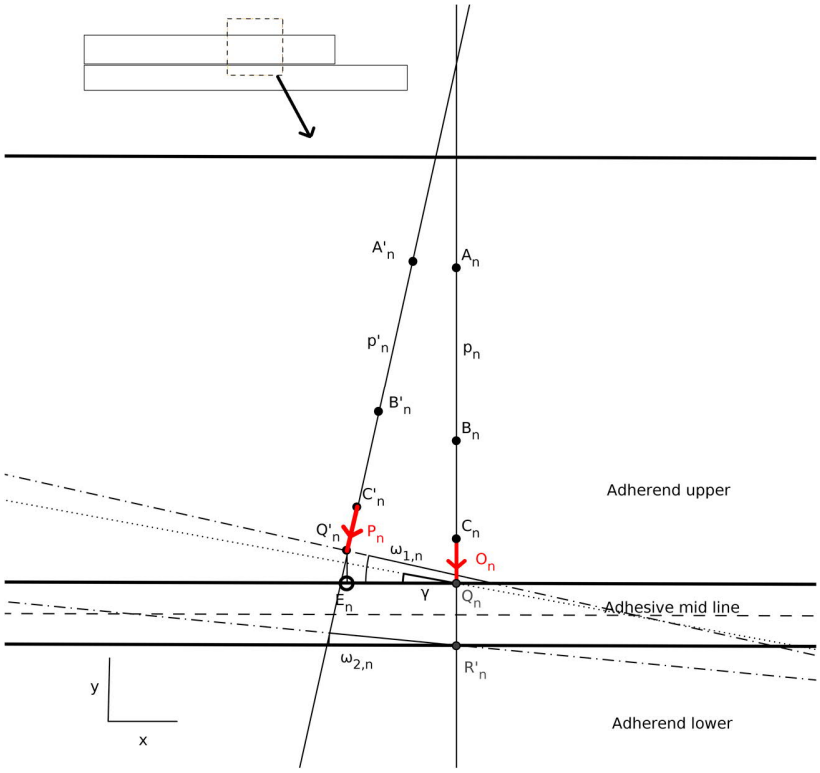

Figure 5: An illustration of a deformed specimen and the control/reference points used in the DIC data analysis.

A similar procedure is then performed for the lower adherend to determine $\boldsymbol{R'_n}$ or the location of the contact point between the lower adherend and the adhesive. Finally, the deformed adherend–adhesive contact points are obtained throughout the region of interest along the x-axis for each n.

During loading, the adherends rotate to angles $\omega_{1,n}$ and $\omega_{2,n}$ Thus, for a thin adhesive layer its mid-line rotation can be defined with:

$$\alpha = (\omega_{1,n} + \omega_{2,n})/2. \tag{4}$$

Taking the rigid body rotations into account, as described in detail by Hogberg et al. [20], we can determine the shear (v) and opening (w) deformations of the adhesive bond line in a (x,y) coordinate system with the known rotation:

$$v = v_0 \cos\alpha + (w_0 + t)\sin\alpha\,, \tag{5}$$

$$w = (w_0 + t)\cos\alpha - v_0 \sin\alpha - t \tag{6}$$

where $v_0 = \|\boldsymbol{E_n Q_n}\|$, $w_0 = \|\boldsymbol{Q'_n E_n}\|$ and $t = \|\boldsymbol{Q_n R'_n}\|$.

Finally, the engineering shear strain (γ_{xy}) and opening (ε_{yy}) strains over the whole adhesive bond line and from each DIC image are calculated as follows:

$$\gamma_{xy} = v/t \tag{7}$$

and

$$\varepsilon_{yy} = w/t \tag{8}$$

2.4. FE analysis and VCCT

FE models representing SLBa, SLBb and ENF specimens were created using Abaqus/Standard 2017 (Dassault Systemes). The adhesive layers were included in addition to the aluminium adherends of the specimens. Adhesive and adherend parts were joined using the tie constraint. This allowed the usage of dissimilar meshes between the adhesive and the adherend. The applied FE models were modelled using 3D solid elements. The elements were C3D8R and C3D8I for the adherend and adhesive parts respectively. The typical element dimension in the adherend and adhesive parts were 2.5 mm and 0.35 mm respectively. Typical element size was constant throughout the adhesive and adherend and no mesh grading was applied. ENF and SLBa element meshes are shown in Fig. 6. The SLBb mesh was practically similar

than SLBa excluding difference in adhesive element thickness. The VCCT was used for analysing the ERR in all of the tested specimens. The VCCT was originally developed by Kanninen and Rybicki [21] and is based on Irwin's crack closure integral. The VCCT has been used in the analysis of various bonded joints [22, 23, 24]. The VCCT evaluates the momentary ERR using the reaction force at the crack tip and the separation of displacements next to the crack tip. The ERR for mode II can be extracted from the equation:

$$G_{II} = \frac{F\delta u}{2B\delta a}, \tag{9}$$

where F is the (nodal) reaction force, δu is the separation, and B and δa are the width and the element length respectively. The VCCT evaluates other fracture modes in a similar way. The interface required by the VCCT was modelled at the midline of the adhesive part, which also equals the 'cohesive' debond surface (which is between two adhesive film plies in reality).

Boundary conditions of ENF and SLBa are presented in Figure 6. All three models had boundary conditions in two locations. These locations presented supporting boundary conditions at the specimen bottom (Figs. 2 and 3). The boundary conditions were defined using partition lines for the whole width of the model. The boundary condition (the precrack side) allowed the translation in the longitudinal direction of the specimen while others were restricted. Another supporting boundary condition had all translations restricted. The loading was attached to the nodal line at the longitudinal middle of the specimen to the opposite side the boundary conditions. The loading presenting the experimental average force was divided into nodal points using the concentrated force in the FE analysis.

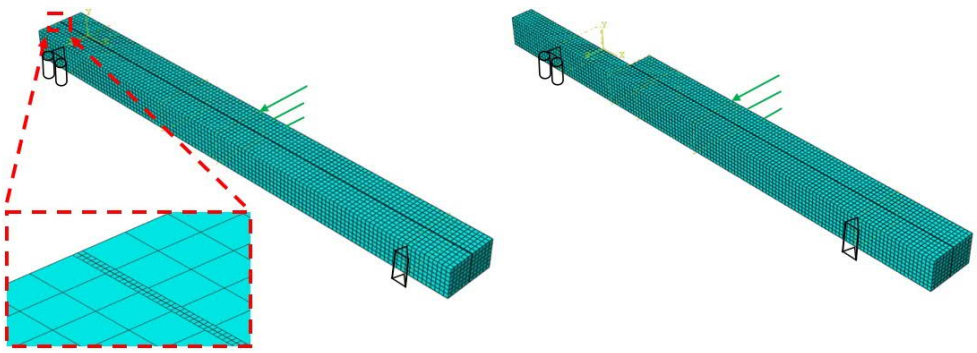

Figure 6: ENF and SLBa specimen models with the applied FE mesh and boundary conditions.

3. Results

3.1. Fracture test results

The post-test fracture surfaces for the SLBa and SLBb specimens are shown in Fig. 7. The fracture type in all the specimens was cohesive. The force-displacement curves of the ENF, SLBa and SLBb experiments are shown in Figs. 8, 9 and 10. The curves show a common trend. The curves first reach a peak value, which is followed by a force drop caused by the crack onset and propagation. The force growth continues soon after the drop. The unloading curve of one specimen in the SLBa testing and for all of the ENF specimens was not recorded.

Figure 7: Fracture surface fractography of SLBa (left) and SLBb (right) specimens after testing.

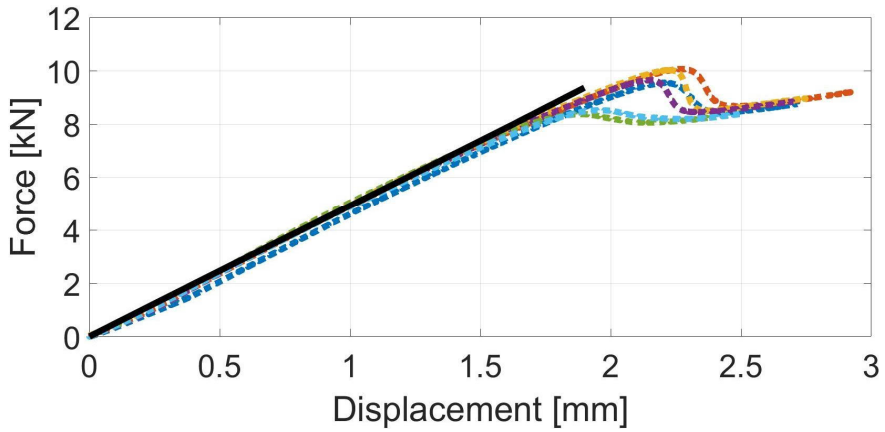

Figure 8: ENF force-displacement curves, based on the experimental tests (the dotted line) and FE analysis (the solid line).

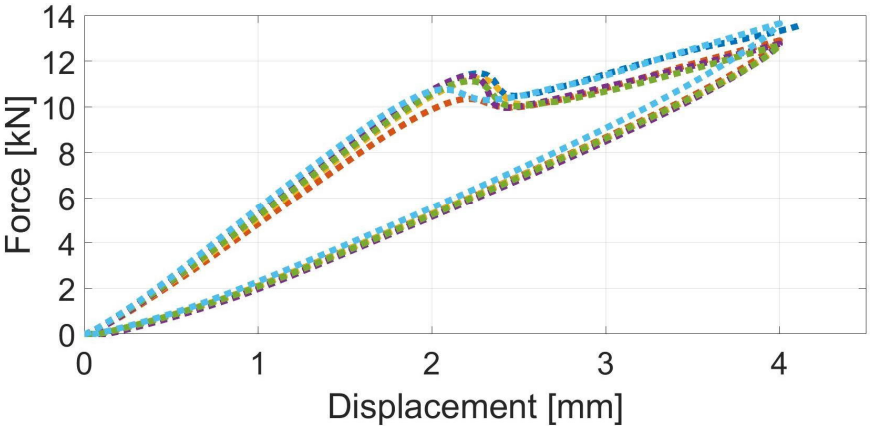

Figure 9: The SLBa force-displacement curves from the experimental tests.

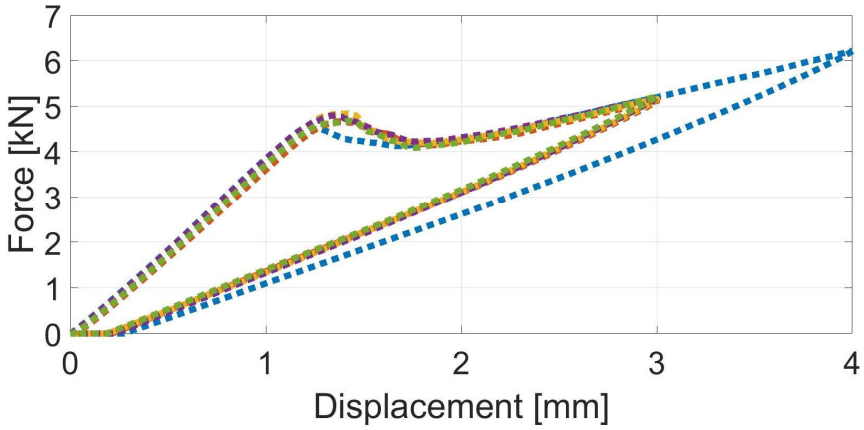

Figure 10: SLBb force-displacement curves from the experimental tests.

A strain gauge was located in the middle point in the tension side of the SLBa and SLBb specimens. The SLBa and SLBb related force-strain curves are shown in Figs. 11 and 12. The specimen 2 strain gauge was observed to have broken and the strain could not be read (SLBa testing). All the curves remain essentially linear up to the peak load.

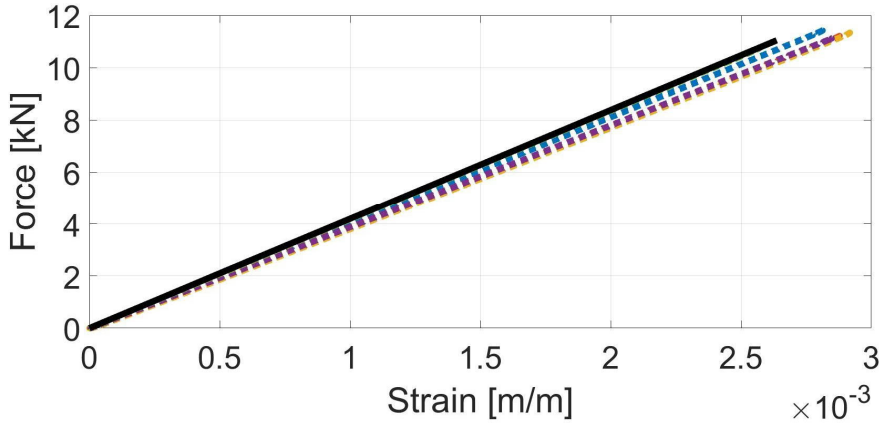

Figure 11: SLBa experimental force-strain curves (the dotted line) and FE analysis maxima (the solid line).

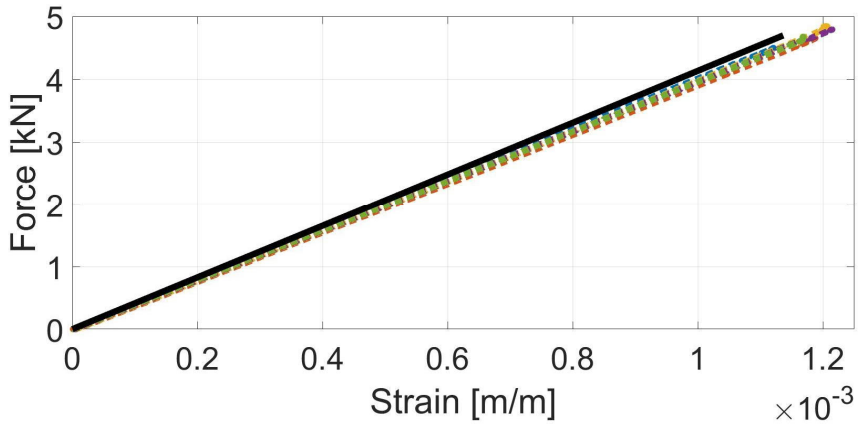

Figure 12: SLBb experimental force-strain curves (the dotted line) and FE analysis force-strain curves (the solid line).

The average experimental peak load before the drop applied in the FE analysis are presented in Table 1. These force values were used in the ERR analysis per each test. The response of the FE analysis model was compared to the experimental force-displacement curves of the ENF testing and the force-strain curves of the SLBa and SLBb experiments. These VCCT results are shown in Figs. 8, 11 and 12. The comparison between the FE and experimental curves shows a good correlation in terms of the specimen

stiffness. The FE provides slightly stiffer behaviour than the experimental curves due to the negligible non-linearities during the experiments.

Table 1: The average experimental peak load applied in the FE analysis per test series.

	SLBa	SLBb	ENF
Peak load before the drop [N]	11,045 ± 419	4,696 ± 134	9,362 ± 739

3.2. Mixed-mode specimens DIC analysis

Figs. 13a and 13b show the full-field strain maps of the vertical strains (ε_{yy}) (opening or compressive) and Figs. 14a and 14b show the shear strains (ε_{xy}) for typical SLBa and SLBb specimens right before the initiation of the crack propagation. In the SLBa test, a small compressive strain is generated at the tip of the upper adherend specimen due to the slightly different curvatures of the adherends around the pre-crack area (when the specimen was loaded). The upper adherend's free end thus acts as a local constraint during bending, also causing slight opening-type (mode I) deformation in the crack-tip locus in addition to dominant mode II loading in the SLBa. In the SLBb tests, the strain distributions are more symmetrical, as seen in Figs. 13b and 14b.

a)

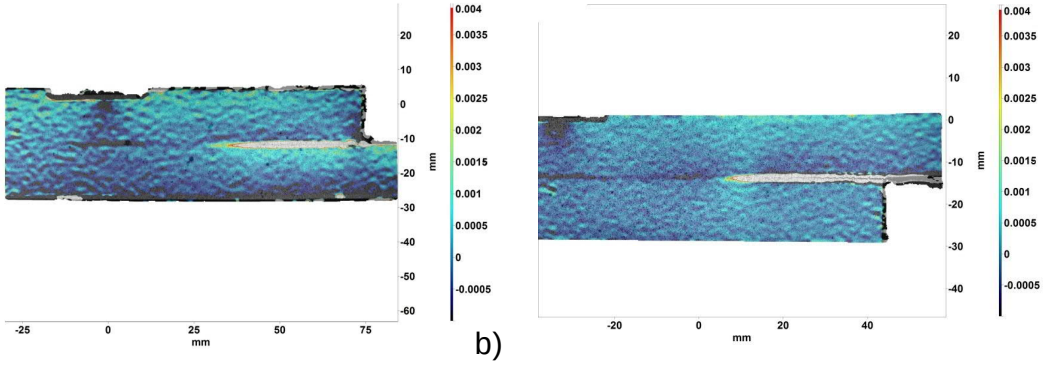

b)

Figure 13: The strain (ε_{yy}) on (a) an SLBa specimen at 57 s (10.4 kN) and (b) an SLBb specimen at 35 s (4.2 kN).

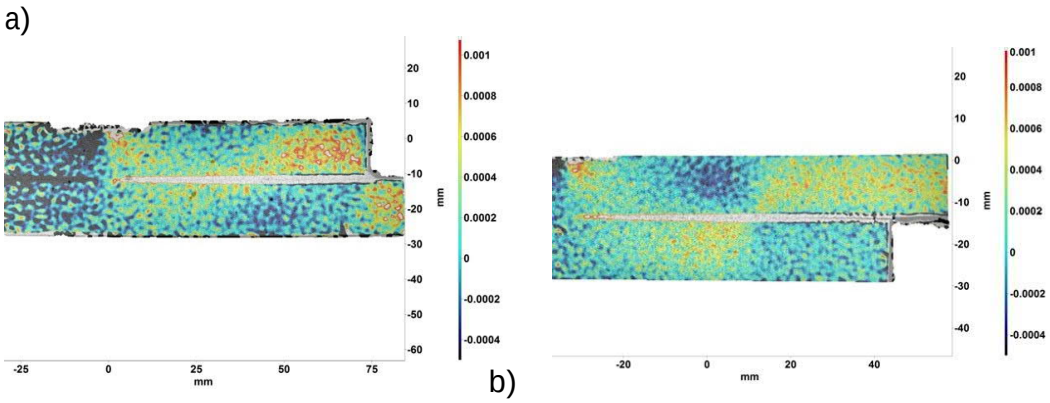

Figure 14: The strain (ε_{xy}) on (a) an SLBa specimen at 57 s (10.4 kN) and (b) an SLBb specimen at 35 s (4.2 kN).

The shear and opening deformations of the selected median specimens, calculated by Eqs. 5 and 6, are presented at the time of the crack propagation onset along the adhesive layer in Fig. 15. Although, in the SLBa-type test, there is a significant amount of opening deformation, the shear deformation is the dominating deformation mode throughout the bond line. In the SLBb-type test, it is seen that, near the crack tip (< 5 mm), the opening deformation exceeds the shear deformation. It is also seen that, in this test type, the opening of the adhesive bond changes into a small compressive deformation at an approximately 11 mm distance from the crack tip.

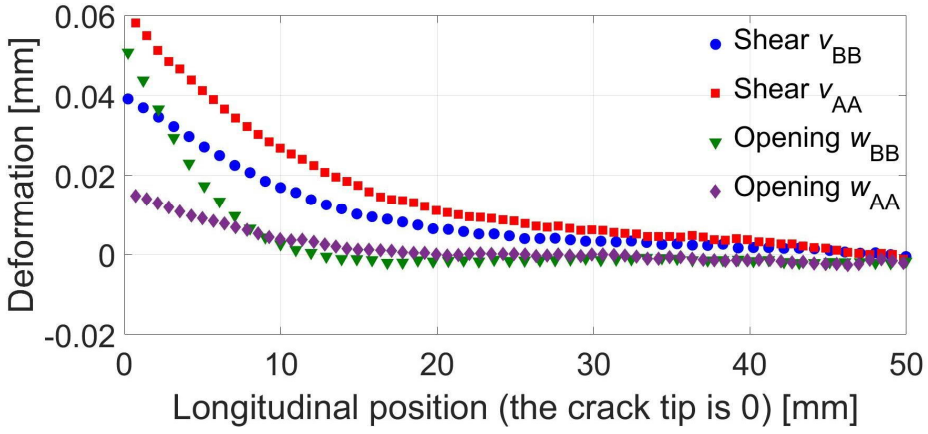

Figure 15: Experimental shear and opening deformations in the adhesive layer in the SLBa and SLBb specimens.

The resolved shear and opening strains determined with Eqs. 8 are shown in Figs. 16 and 17. The figures also include the strains provided by the FE analysis, which are needed for an accurate ERR determination. The comparison of the DIC- and FE-based shear strains of the adhesive shows good correlation. However, the comparison of the opening strain indicates significant difference between the two methods. The DIC provided greater values when compared to the FE analysis. The fracture surface revealed that the release film used to prepare the pre-crack (thickness: 20 µm) had wrinkled during the specimen manufacturing. An optical profilometer image of an SLBa specimen (Fig. 18) shows the waviness of the pre-crack area to have a peak-to-peak amplitude of approximately 100 µm. The small scale sliding of the adherends free ends during bending with the observed wavy surface topography causes some local constraint for the system. This, at least partly, can explain the difference between the experiments and the simulation because in FE the pre-crack surfaces are assumed to be smooth and sliding relative to each other without any surface asperities hindering the process.

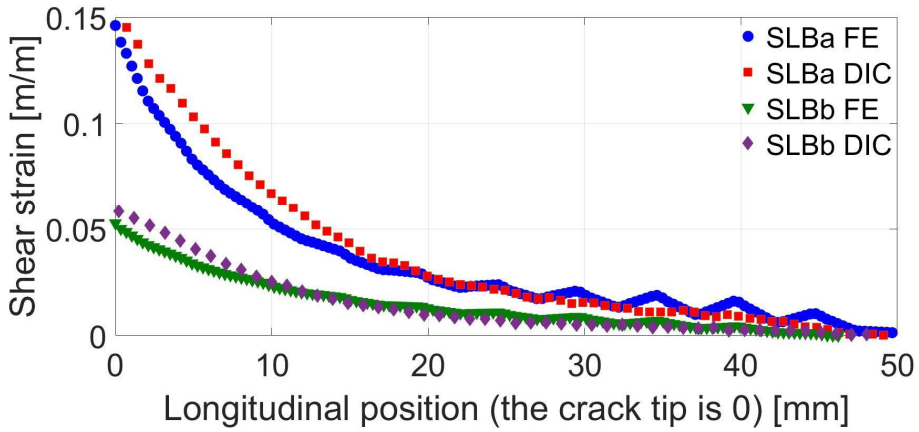

Figure 16: Shear strain in the adhesive layer in the SLBa and SLBb specimens at crack onset.

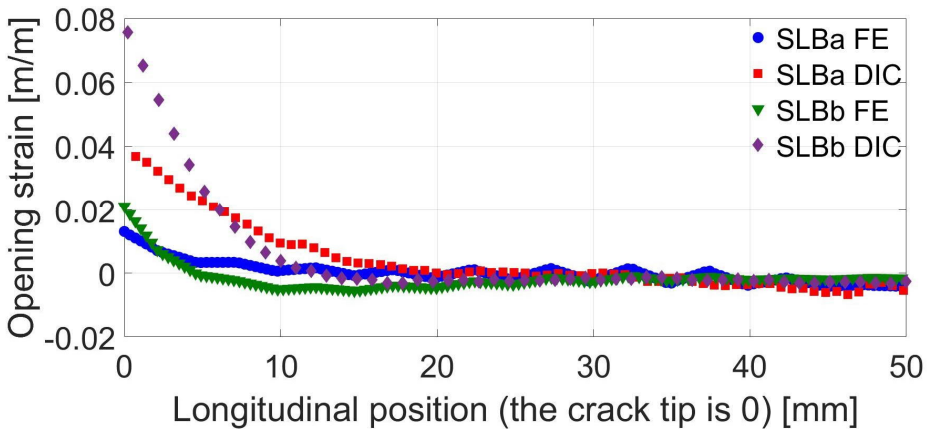

Figure 17: Opening strain in the adhesive in the SLBa and SLBb specimens at crack onset.

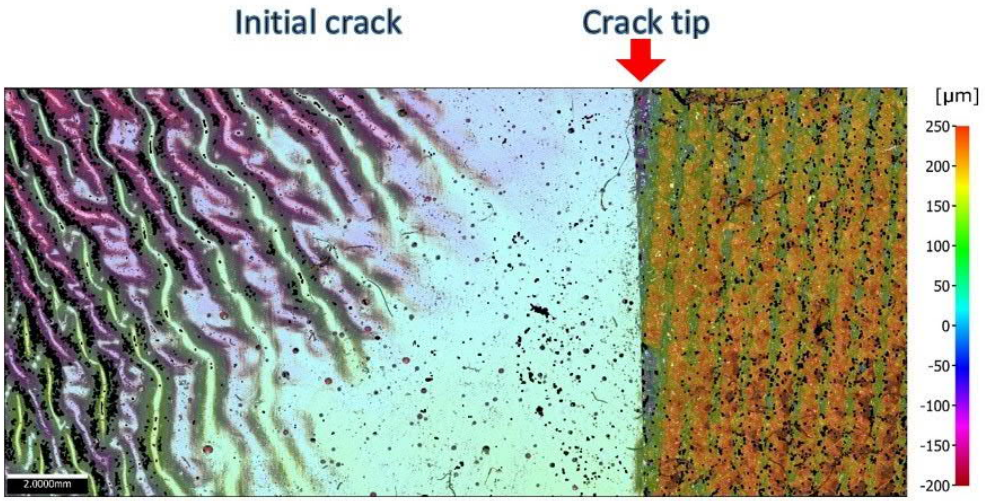

Figure 18: Surface topography measured by using a profilometer close to the pre-crack tip of an SLBa specimen.

3.3. Mixed-mode fracture criterion

The VCCT analyses were performed for all the three specimen types. The VCCT evaluated the ERR distributions at the 3D crack tip, and these results are shown in Fig. 19. Fig. 19 presents the mode I and mode II values for the SLBa and SLBb specimens. Pure mode II is presented for the ENF specimen. The mode II distributions have the highest values at the outer edges of the

specimens in contrast to the fracture mode I. Specimen ERR distributions should be presented with one value when determining the criterion. The middle point (line) value of the distribution was chosen to be representative. This selection basically follows the plane strain assumption, which is typically used in two-dimensional FE analyses. The middle nodal point values are collected into Table 2, which also presents the mode I DCB result [14].

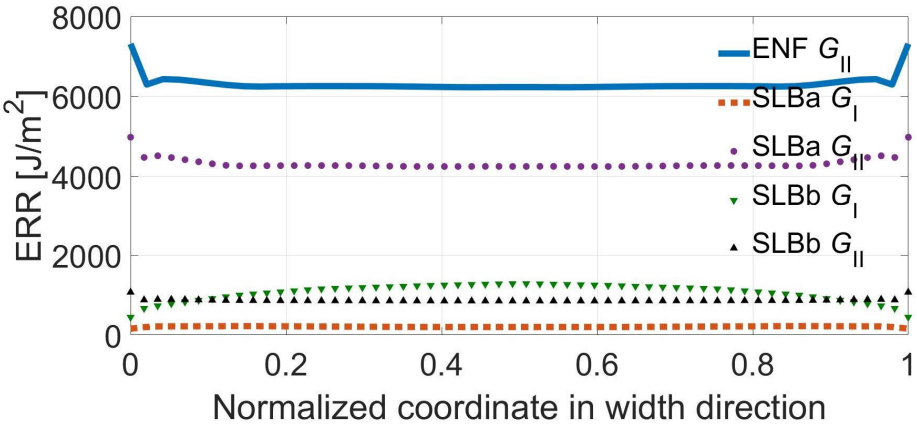

Figure 19: Energy release rate distributions for ENF, SLBa and SLBb specimens and test types.

Table 2: A summary of the fracture test–given ERR values at crack onset.

	DCB	SLBa	SLBb	ENF
G_I [J/m²]	1820	200	1285	0
G_{II} [J/m²]	0	4250	850	6230

Based on the defined ERR values (Table 2), curve fitting for the power law criterion was determined. The least square method fitting was performed using Isight software (Dassault Systemes). Fittings were performed for unequal α and β, and also with equal values ($\alpha = \beta$). The results of the fitting survey are shown in Fig. 20. In addition, the experimental results and the typically used linear criterion is shown (Fig. 20). Based on the results, the power law defined by SLBa and SLBb specimens undoubtedly improves the accuracy of the interaction between pure modes I and II for mixed loadings.

The linear power law is shown to be non-conservative and the difference between these fits is almost 20 percent.

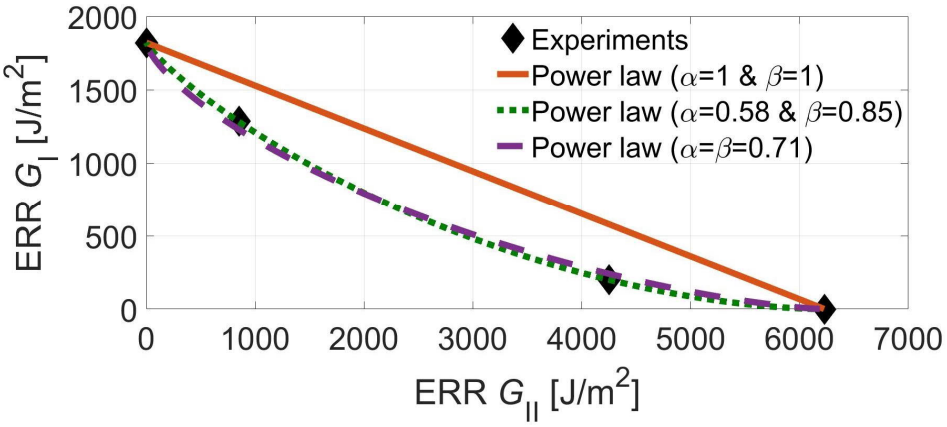

Figure 20: The developed fracture criterions for linear fit and power law (unequal α and β and equal (α=β)).

4. Discussion

The usage of one common specimen design in a single loading condition only provides a single-mode ratio value. More ratios can be achieved when dimensions are modified per specimen design. In this work, two different mixed-mode ratios are achieved using a single specimen design without changing any dimensions of the specimen. The applied specimen geometry is simple from the manufacturing point of view. The specimen is loaded under three-point bending, which does not require the use of a complex testing jig (e.g. as in MMB testing). Basically, the specimen geometry and the induced loading are relatively similar to the ENF specimen testing.

The established testing method in the composite laminate mixed-mode delamination testing is the MMB [8]. The MMB includes a complex loading jig where the ratio between modes can be varied – this being an advantage. The fracture processes of structural joints are typically much more ductile than a composite interlaminar fracture. This results in having thicker adherends with which to avoid adherend plastic deformation. Elastic adherend deformation is typically required for standard material properties to be evaluated. The increase in the specimen size, in turn, requires higher loading, which should be taken into account when designing the loading jig. For that

reason, the adhesive mixed-mode testing should aim for test with simpler specimens and testing fixture [25].

The target of the testing was also to define the fracture criterion for FM 300-2. Tenchev and Falzon [26] stated that power law exponents are typically between 1 and 2. Donough et al. [27] applied FM 300-2K in experiments and an analysis of a single lap joint and skin-doubler joints. They used a quadratic power law criterion in their analysis. Kim et al. [28] used an exponent value of 1 when analysing scarf joints under in-plane loading and impact. In the current literature, both Donough et al. [25] and Kim et al. [26] presumed the order of the criterion, i.e. did not find the value of exponent based on experimental data. Based on literature, power law exponents are mainly assumed to have value of 1 or 2. The exponent values determined in this study were less than 1. This means that the typical assumptions used in the literature do not provide conservative results under mixed-mode conditions for the current adhesive. The usage of the exponent value of 2 makes the situation even less conservative.

The maximum shear strains determined by DIC were roughly 0.15 and 0.05 in the SLBa and SLBb specimens respectively. The material data sheet of FM 300-2K [29] provides 0.093 and 0.544 for knee and ultimate strains (knee of the curve stands for significant change in slope of stress-strain curve). Duong and Wang provided the values 0.083 and 0.3 for elastic and maximum shear strains [30]. Here, the maximum measured strains in the SLBa specimens are close to the linear and knee strains found from literature. However, there is a difference when compared to the ultimate shear strains. It can be assumed that, very near the existing crack tip, the strains are higher, but this cannot be detected by the utilised DIC method due to restricted spatial resolution. Generally, the stress-strain behaviour of adhesive shear properties is studied using the TALS specimen. The shear deformation in these specimens are distributed more smoothly than in the SLB specimens in this study. Of course, this also minimises the mode I fracturing at the crack tip, which was not the target of the SLBa testing.

5. Conclusion

In this work, an alternative concept for defining the adhesive mixed-mode criterion is developed. The approach relies on a simple mixed-mode specimen design (SLBa, SLBb) that is loaded under the three-point bending condition. The specimen usage provides two different mode ratios. For a

complete criterion, DCB and ENF tests are typically performed alongside each other – as they are in this work. The fracture criterion for the epoxy film adhesive FM 300-2 was defined with this approach. The power law criterion exponents' values were determined to be 0.58 and 0.85 for modes I and II respectively and 0.71 when having equal exponents for both modes. The new criterion provides lower values under mode-mixity conditions compared to the typically used criterion with linear exponents.

Here, DIC was applied for the mixed-mode testing in order to understand the precise mixed-mode loading of the adhesive. Because the DIC was not able to directly determine strain distributions at the adhesive bond line (thickness 0.4–0.67 mm), the DIC output was post-processed using adherend reference points for determining (shear) strains in the adhesive. The enhanced DIC analysis revealed the opening strains in the SLBb specimen and in the SLBa specimen. The comparison of strain components amidst the crack tip showed that the opening strains (defined by FE and DIC) differ significantly while the shear strains had good correlation.

6. Acknowledgements

This work was funded by the financial support of the Finnish Defence Forces Logistics Command. The technical support offered by the CSC–IT Center for Science Ltd (Finland) is gratefully appreciated.

7. References

[1] D. A. Dillard, H. K. Singh, D. J. Pohlit, J. M. Starbuck, Observations of decreased fracture toughness for mixed mode fracture testing of adhesively bonded joints, Journal of Adhesion Science and Technology, 23 (2009), 1515-1530

[2] M. L. Benzeggagh, M. Kenane, Measurement of mixed-mode delamination fracture toughness of unidirectional glass/epoxy composites with mixed-mode bending apparatus, Composite Science and Technology 56 (1988) 439–449.

[3] J. R. Reeder, An evaluation of mixed-mode delamination failure criteria, NASA Technical Memorandum 104210, 1992.

[4] R. L. Ramkumar, Performance of a quantitative study of instabilityrelated delamination growth, NASA Contractor Report 166046, 1983.

[5] Dassault Systemes, Abaqus 2017 Documentation, User manual, 2017.

[6] ISO 25217, Adhesives – Determination of the mode 1 adhesive fracture energy of structural adhesive joints using double cantilever beam and tapered double cantilever beam specimens, International Organization for Standardization, 2009.

[7] S. Marzi, O. Hesebeck, M. Brede, F. Kleiner, An end-loaded shear joint (ELSJ) specimen to measure the critical energy release rate in mode II of tough, structural adhesive joints, Journal of Adhesion Science and Technology, 23 (2009), 1883-1891

[8] ASTM D6671, Standard Test Method for Mixed Mode I-Mode II Interlaminar Fracture Toughness of Unidirectional Fiber Reinforced Polymer Matrix Composites, American Society for Testing and Materials, ASTM, 2006.

[9] S. Park, D. A. Dillard, Development of a simple mixed-mode fracture test and the resulting fracture energy envelope for an adhesive bond, International Journal of Fracture 148 (2007) 261–271.

[10] B. R. K. Blackman, A. J. Kinloch, F. S. Rodriguez-Sanchez, W. S. Teo, The fracture behaviour of adhesively-bonded composite joints: Effects of rate of test and mode of loading, International Journal of Solids and Structures 49 (2012) 1434–1452.

[11] H. L. J. Pang, C. W. Seetoh, A compact mixed mode (CMM) fracture specimen for adhesive bonded joints, Engineering Fracture Mechanics 57 (1997) 57–65.

[12] T. N. Chakherlou, S. R. Hakim, A. Mohammadpour, H. N. Maleki, A. B. Aghdam, Experimental and numerical investigations of crack face adhesive bonding effect on the mixed-mode fracture strength of PMMA, Journal of Adhesion Science and Technology, 30 (2016), 2236-2256

[13] M. V. Fernandez, M. F. S. F. de Moura, L. F. M. da Silva, T. Marques, Mixed-mode I + II fatigue/fracture characterization of composite bonded joints

using the Single-Leg Bending test, Composites Part A: Applied Science and Manufacturing 44 (2013) 63–69.

[14] J. Jokinen, M. Wallin, O. Saarela, Applicability of VCCT in mode I loading of yielding adhesively bonded joints – A case study, International Journal of Adhesion and Adhesives 62 (2015) 85–91.

[15] O. Ishai, H. Rosenthal, N. Sela, E. Drukker, Effect of selective adhesive interleaving on interlaminar fracture toughness of graphite/epoxy composite laminates, Composites 19 (1) (1988) 49–54.

[16] J. Aakkula, J. Jokinen, O. Saarela, S. Tervakangas, Testing and modelling of DIARC plasma coated elastic-plastic steel wedge specimens, International Journal of Adhesion and Adhesives 68 (2016) 219–228.

[17] E. M. C. Jones, M. A. E. Iadicola, A Good Practices Guide for Digital Image Correlation, International Digital Image Correlation Society, DOI:10.32720/idics/gpg.ed1, 2018.

[18] M. Bornert, F. Bremand, P. Doumalin, J.-C. Dupre, M. Fazzini, M. Grediac, F. Hild, S. Mistou, J. Molimard, J.-J. Orteu, L. Robert, Y. Surrel, P. Vacher, B. Wattrisse, Assessment of Digital Image Correlation Measurement Errors: Methodology and Results, Experimental Mechanics 49 (2009) 353–370.

[19] M. Rossi, P. Lava, F. Pierron, D. Debruyne, M. Sasso, Effect of DIC Spatial Resolution, Noise and Interpolation Error on Identification Results with the VFM, Strain 51 (2015) 206–222.

[20] J. L. Högberg, B. F. Sørensen, U. Stigh, Constitutive behaviour of mixed mode loaded adhesive layer, International Journal of Solids and Structures 44 (2007) 8335–8354.

[21] E. F. Rybicki, M. F. Kanninen, A finite element calculation of stress intensity factors by a modified crack closure integral, Engineering Fracture Mechanics 9 (4) (1977) 931–938.

[22] G. Marannano, L. Mistretta, A. Cirello, S. Pasta, Crack growth analysis at adhesive-adherent interface in bonded joints under mixed mode I/II, Engineering Fracture Mechanics 75 (2008) 5122–5133.

[23] R. K. Behera, S. K. Parida, R. R. Das, Effect of the aspect ratio of the pre-existing rectangular adhesion failure on the structural integrity of the adhesively bonded single lap joint, Journal of Adhesion and Technology, 33 (2019), 2093-2111

[24] J. Jokinen, M. Kanerva, M. Wallin, O. Saarela, The simulation of a double cantilever beam test using the virtual crack closure technique with the cohesive zone modelling, International Journal of Adhesion and Adhesives 88 (2019) 50–58.

[25] G. G. Tracy, P. Feraboli, K. T. Kedward, A new mixed mode test for carbon/epoxy composite systems, Composites: Part A 34 (2003) 1125–1131.

[26] R. T. Tenchev, B. G. Falzon, Experimental and numerical study of debonding in composite adhesive joints, 16th International Conference on Composite Materials, Kyoto, Japan, 2007.

[27] M. Donough, A. Gunnion, A. Orifici, C. Wang, Critical assessment of failure criteria for adhesively bonded composite repair design, Proceedings of the 28th Congress of the Aeronautical Sciences, Brisbane, Australia, 2012.

[28] M. K. Kim, D. J. Elder, C. H. Wang, S. Feih, Interaction of laminate damage and adhesive disbonding in composite scarf joints subjected to combined in-plane loading and impact, Composite Structures 94 (2012) 945–953.

[29] FM 300-2 film adhesive, Technical data sheet, Cytec Engineered Materials, 2011.

[30] C. N. Duong, C. H. Wang, Composite repair Theory and design, Elsevier, 2007.